Case Studies in Thermal Engineering 86 (2026) 108491

Contents lists available at ScienceDirect

Case Studies in Thermal Engineering

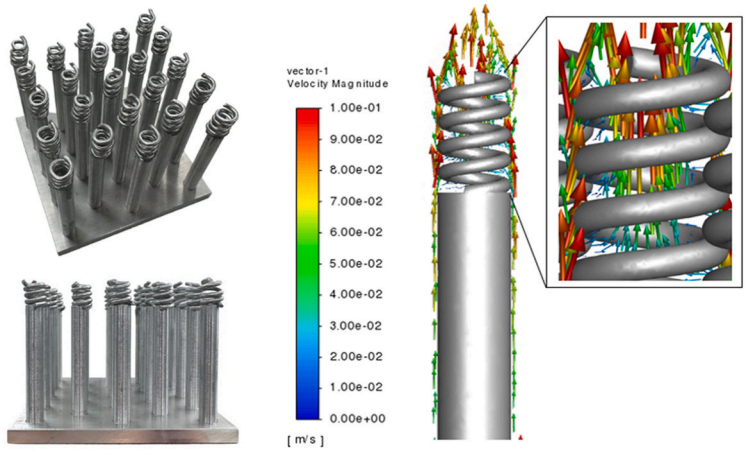
journal homepage: www.elsevier.com/locate/csite

Improvement in natural convection cooling performance of a heatsink by replacing the upper section of cylindrical pin fins with a spring structure

Hyeon-Min Kang, Se-Jin Yook *

School of Mechanical Engineering, Hanyang University, Seoul, 04763, Republic of Korea

GRAPHICAL ABSTRACT



ARTICLE INFO

Keywords:
Pin fin heatsink
Natural convection
Thermal resistance
Optimization
Spring

ABSTRACT

Natural convection-based cooling technology has attracted considerable attention as a promising approach for achieving both lightweight characteristics and efficient thermal management in electronic devices and energy systems. In this study, a novel heatsink in which the upper portions of conventional cylindrical pin fins were replaced with spring structures was proposed, and its thermal performance in naturally convective flow conditions was evaluated through numerical and experimental analyses. The wire diameter, height, and pitch of the spring were selected as

* Corresponding author.
E-mail address: ysjnuri@hanyang.ac.kr (S.-J. Yook).

https://doi.org/10.1016/j.csite.2026.108491
Received 31 May 2026; Received in revised form 26 August 2026; Accepted 31 August 2026
Available online 2 September 2026
2214-157X/© 2026 The Authors. Published by Elsevier Ltd. This is an open access article under the CC BY-NC license (http://creativecommons.org/licenses/by-nc/4.0/).

design variables, and optimization was carried out employing the Response Surface Methodology (RSM) based on numerical results. The findings revealed that the spring height was the dominant parameter affecting thermal resistance. Under the optimal conditions of a diameter of 1.25 mm, height of 10 mm, and pitch of 2.2 mm, the difference between the RSM prediction and numerical result was only 0.72%, confirming the accuracy of the model. Compared with the reference heatsink composed only of cylindrical pin fins, the optimized cylindrical-spring pin fin heatsink reduced thermal resistance by 10.4% while decreasing mass by 5.7%. Flow field analysis revealed that the spring structure promoted fluid mixing and accelerated upward flow through the interaction between the internal core flow and external side flow, facilitating natural convection heat transfer enhancement. The experimental and numerical outcomes agreed with a discrepancy of less than 5.14%, while the maximum experimental uncertainty was evaluated as 5.83%. The proposed cylindrical-spring pin fin heatsink is anticipated to offer a promising design strategy for simultaneously improving cooling performance and reducing weight.

1. Introduction

Amid global efforts toward sustainable development, the reduction of energy consumption has been recognized as a critical issue, and improvement of energy efficiency in the lighting sector has occupied a particularly important position. Lighting contributes to about 17% of global electricity consumption [1], and approximately 15% of the electricity generated in the power production sector, which is responsible for nearly 30% of total CO_2 emissions, is consumed for lighting purposes [2]. Therefore, the necessity for energy savings in this field is considerable. Under these circumstances, light-emitting diodes (LEDs), which demand only approximately one-tenth of the electrical power required by conventional light sources, have rapidly expanded as a key lighting technology replacing traditional light sources such as fluorescent and incandescent lamps [3]. However, approximately 70–85% of the supplied electrical power in LEDs is released as thermal energy [4], and the resulting high operating temperature has a direct influence on the maximum luminous output, lifetime, reliability, and color quality [5–7]. Therefore, thermal management in LED packaging is essential, and heatsink design for securing effective heat dissipation performance under natural convection conditions has become an important research topic. Accordingly, various heatsink configurations have been proposed [8–12]. In particular, under natural convection environments favorable for low-cost and compact applications, extensive studies based on pin fin or rectangular fin structures have been conducted. These studies have emphasized the critical role of design optimization for maximizing heat transfer area and improving airflow within limited spaces [13–18]. Recently, various approaches have been investigated to further enhance passive cooling performance through advanced heatsink geometries and heat transfer enhancement techniques. A passive cooling system combining a bio-inspired heatsink with nanoparticle-enhanced phase change material was proposed [19], while the fluid flow and heat transfer characteristics of a micro-channel heatsink equipped with semi-elliptical pin fins were numerically investigated [20]. In addition, the configuration of a longitudinal fin exposed to combined natural convection and radiation was optimized to enhance heat transfer performance [21]. These studies demonstrate that fin configuration, flow-field control, and numerical-analysis-based geometry optimization play important roles in enhancing the thermal performance of passive cooling systems.

Previous studies intended to improve the cooling performance of heatsinks have generally been carried out in two directions. The first approach involved geometric optimization of fin shape and arrangement. Studies employing staggered fin arrangements to induce flow disturbance and promote heat transfer [22,23], as well as studies attempting to lower thermal resistance by altering design parameters such as fin length, installation angle, and fin number, have been reported [24,25]. The second approach involved enhancement of heat transfer by combining additional functional elements with conventional fin structures. For example, Sung et al. [26] additionally installed aluminum rings on each pin fin to induce a chimney effect. As a result, the buoyancy-driven flow was strengthened, and the thermal resistance of the heatsink was lowered by approximately 15.3%. Effendi and Kim [27] proposed a hybrid structure combining radial plate fins around pin fins, thereby enlarging the heat dissipation area and improving airflow, which lowered the thermal resistance of the heatsink by up to 32%. However, these approaches possess limitations associated with increased heatsink weight and increased material consumption due to the addition of extra structures.

To overcome these limitations, studies aimed at simultaneously improving airflow and reducing weight through modification of the fin structure itself have recently been conducted. Park et al. [28] inserted a hollow cylinder at the center of the heatsink to strengthen the chimney effect, and significant performance enhancement corresponding to approximately 43% reduction in thermal resistance was reported. Huang et al. [29] applied perforations directly to the fins to promote air inflow, thereby reducing the thermal resistance of the heatsink by approximately 29.1%. It was also confirmed that such structural modifications provided the additional advantage of weight reduction corresponding to the removed volume while improving heat transfer performance. Meanwhile, the thermal performance of heatsinks strongly depends not only on geometry but also on installation angle. Meng et al. [30] confirmed that the cooling performance was enhanced by 6.88% when the heatsink was installed vertically. Elshafei [31] compared solid fins and hollow fins and reported that both configurations exhibited superior cooling performance in the vertical orientation. In particular, hollow fins showed more effective performance under identical heat load conditions. These studies emphasized the importance of internal flow path formation and natural convection flow. However, hollow and perforated structures possess limitations in that complex manufacturing processes and additional machining steps are required.

To address these issues, a spring structure capable of simultaneously securing complex flow paths and high specific surface area while maintaining a simple manufacturing process was introduced in the present study. The spring structure can naturally form

internal flow paths through its continuous curved geometry and is structurally advantageous for lightweight design. Biswal et al. [32] reported that natural convection heat transfer performance was improved as the spring diameter and pitch increased even under the same total surface area condition, indicating that geometric parameter variation promoted internal flow. In addition, under high Rayleigh number conditions, cold air entering from the bottom and sides was introduced into the coil center, while heated air was rapidly discharged upward, thereby forming a strong chimney effect that maximized cooling performance at the center region [33]. These findings demonstrate that the spring structure possesses the potential to naturally induce chimney-effect-enhanced natural convection upward flow and improve heat transfer performance without requiring additional complex processing. Therefore, in the present study, a novel design in which a portion of the conventional circular pin fin heatsink structure was replaced with aluminum spring wire was proposed to simultaneously achieve weight reduction and enhancement of thermal performance. In addition, through thermal-flow analysis and experimental validation, the performance and applicability of the proposed structure were quantitatively evaluated in order to clearly present a differentiated design concept and engineering validity compared with previous studies. Unlike conventional hollow and perforated fin structures, which require additional machining steps to form internal flow paths, the cylindrical-spring pin fin proposed in the present study replaced the upper section of a conventional cylindrical pin fin with aluminum spring wire, thereby forming an open internal flow path without additional machining. Furthermore, unlike conventional designs in which the entire fin is composed of a coil structure or a separate chimney structure is employed, the proposed design maintained the heat transfer path through the cylindrical lower section while simultaneously inducing external side flow into the spring and chimney-effect-enhanced upward flow through the spring upper section. Thus, the proposed cylindrical-spring pin fin is differentiated from conventional structures by its hybrid configuration combining the advantages of the cylindrical lower section and spring upper section. The primary objective of the present study was to derive an optimal spring configuration for minimizing thermal resistance by considering the wire diameter, height, and pitch as design variables. The secondary objectives were to compare the heat dissipation performance and flow characteristics of the optimized cylindrical-spring pin fin heatsink with those of the reference model and to evaluate the heat dissipation performance under variations in input power and installation angle from 0° to 180° through numerical and experimental analyses.

2. Numerical method

The structure selected for analysis in the present study was a pin fin heatsink incorporating spring-shaped aluminum wire, and its geometric configuration is displayed in Fig. 1. The heatsink was constructed based on a square base having a thickness of 5 mm and a side length of 75 mm, and a total of 23 fins were arranged at regular intervals on the upper surface of the base. These fins were positioned in a staggered pattern with a spacing of 15 mm in order to effectively induce natural convection flow. To ensure consistency in the comparative analysis, the overall dimensions and basic configuration of the heatsink were identically established to those of the pin fin heatsink used in the study of Kim [34]. The fin configuration developed in the present study possessed a composite structure in which the lower section was cylindrical, whereas the upper section was formed as a spring by coiling aluminum wire. Through this design, the formation of internal flow paths and the increase in specific surface area were simultaneously induced by only a simple structural modification. The geometric characteristics of the spring structure were defined using the wire diameter (d), pitch (p), and height (h) as the principal design variables, and the effects of these parameter variations on flow characteristics and free convection heat transfer were investigated. Meanwhile, the diameter of the fin composed of the cylindrical and spring sections was set to 6 mm, and the total fin height was maintained at 50 mm to enable direct performance comparison with previous studies.

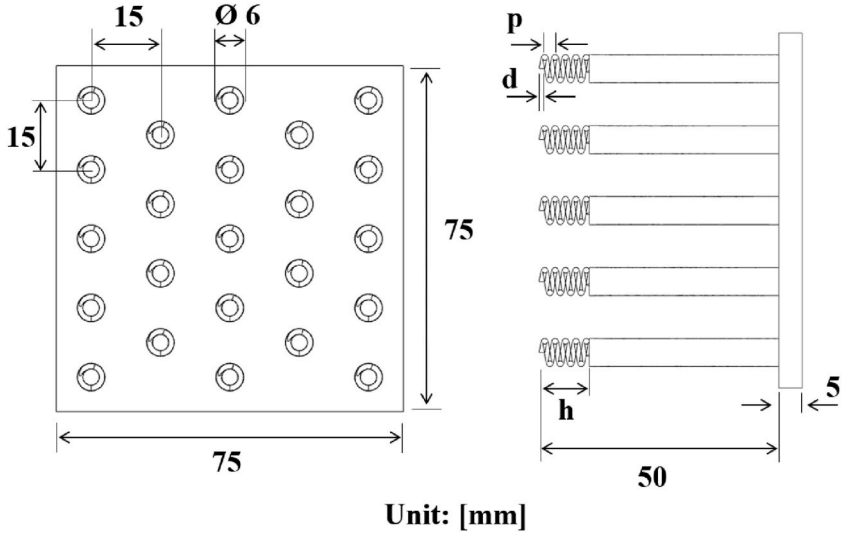


Fig. 1. Geometric configuration and design parameters of the pin-fin heatsink with fins composed of a cylindrical lower section and an aluminum wire spring upper section.

To investigate the thermal and flow behaviors near the proposed heatsink, numerical simulations were conducted employing ANSYS FLUENT *Release 18.1*. Fig. 2 displays the computational domain, which was established with dimensions of 200 mm × 250 mm × 250 mm. The effectiveness of the heatsink was evaluated by altering the installation angle (θ) referenced from the x-axis, and Fig. 2 presents the simulation domain for the case of an installation angle of $\theta = 0°$. The flow was considered to be laminar, steady, and incompressible, and the buoyancy effect induced by natural convection was modeled using the Boussinesq approximation [35]. In this study, the maximum temperature difference between the heatsink and the ambient air was observed for the reference model composed only of cylindrical pin fins without the spring structure at a heat input of 30 W and an installation angle of 180°, and was approximately 86 K. In a previous study [36], the Boussinesq approximation was compared with a variable-property model considering temperature-dependent thermophysical properties under natural convection conditions with temperature differences of up to approximately 100 K, and the maximum difference in the Nusselt number was reported to be approximately 5%. Therefore, the application of the Boussinesq approximation in the present study was considered reasonable for comparing the heat dissipation performance under different heatsink geometries and installation conditions. Variations in air density with time and space, as well as volumetric expansion effects, were neglected. In addition, the effect of heatsink surface roughness was not considered. Under the aforementioned conditions, the governing equations consisted of the continuity equation, momentum equation, and energy equation, which are written as Eqs. (1)–(3), respectively [37–40]. Here, each variable represents the physical properties of air: $\vec{v}$, P, t, μ, ρ, T, F, C_p, k_a, and S denote the velocity vector, pressure, time, viscosity, density, temperature, gravitational force directed toward the ground, specific heat at constant pressure, thermal conductivity, and source term, respectively. Additionally, u, v, and w represent the velocity components in the x-, y-, and z-directions, respectively.

$$\frac{\partial u}{\partial x}+\frac{\partial v}{\partial y}+\frac{\partial w}{\partial z}=\nabla\cdot\vec{v}=0 \tag{1}$$

$$\rho\frac{Dv}{Dt}=-\nabla P+\mu\nabla^2 v+F \tag{2}$$

$$\rho C_p\frac{DT}{Dt}=k_a\nabla^2 T+\frac{DP}{Dt}+S \tag{3}$$

The boundary conditions for the flow analysis were established as follows. Pressure inlet conditions were imposed on all side surfaces of the simulation domain, whereas pressure outlet conditions were applied to the bottom and top surfaces. No-slip conditions were assigned to all heatsink surfaces, including the cylindrical sections, spring sections, and base. A heat input ranging from 5 to 30 W was applied to the bottom surface of the heatsink base. The surrounding pressure and temperature were set to 101.3 kPa and 300 K, respectively. All components constituting the heatsink were assumed to be made of aluminum 6061. To take into account the influence of radiative heat transfer, the Discrete Ordinates (DO) radiation model was employed. The emissivity of aluminum 6061 can vary considerably depending on the surface condition, degree of oxidation, and surface treatment. An emissivity of approximately 0.1 has

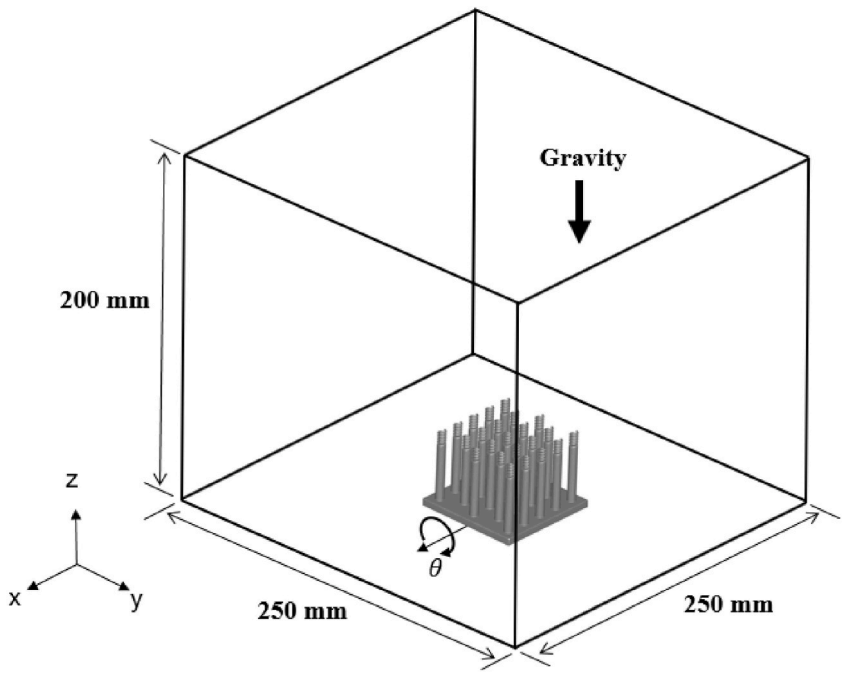


Fig. 2. Computational domain for thermal flow analysis around the heatsink.

been reported for untreated aluminum surfaces, whereas a considerably higher value of up to approximately 0.84 has been reported for anodized aluminum surfaces [41,42]. In the present study, the effect of emissivity on the predicted thermal resistance was evaluated by varying the emissivity from 0.1 to 0.4, and the maximum variation in thermal resistance was found to be approximately 2.3%, indicating that the effect of emissivity on the predicted heat dissipation performance was limited within the investigated range. Therefore, an emissivity of 0.4 was applied to all heatsink surfaces based on the value reported in a previous study [43]. Under these conditions, the heat transfer characteristics involving the combined effects of radiation and free convection were more accurately simulated. To ensure the robustness of the simulation outcomes, a grid independence test was performed [44]. The change of heatsink thermal resistance was analyzed while gradually increasing the mesh element count from about 1 million to 3 million. As a result, the thermal resistance converged within an error of 0.7% independent of grid density when more than approximately 2.5 million grid elements were used. Therefore, considering both computational accuracy and efficiency, a grid system consisting of approximately 2.5 million elements was selected as the optimal condition.

To systematically optimize the spring wire configuration, the Response Surface Methodology (RSM) was employed. RSM is a representative statistical technique capable of constructing an approximate model for the correlation between multiple design variables and system responses based on a limited number of experimental or numerical analysis results. This method possesses the advantage of efficiently reflecting the interaction effects among design variables. Owing to these characteristics, the computational cost and time required for optimal design can be effectively reduced, and thus RSM has been widely utilized in various engineering optimization problems [45]. In the present study, an approximate model based on RSM was constructed from the numerical results to quantitatively analyze the relationship between the principal geometric variables of the spring structure and thermal performance. The correlation between the objective function and independent variables is expressed by Eq. (4) [46]. Here, f denotes the objective function, while a_0, a_i, a_{ij}, and a_{ii} represent the intercept coefficient, linear effect, interaction effect, and quadratic effect, respectively. Additionally, x_i and x_j denote the geometric factors, e signifies the error between the actual and approximated values, and n represents the number of design variables.

$$f = a_0 + \sum_{i=1}^{n} a_i x_i + \sum_{i<j} a_{ij} x_i x_j + \sum_{i=1}^{n} a_{ii} x_i^2 + e \tag{4}$$

The design variable ranges of the spring structure installed on the upper section of the cylindrical portion of the fin were established at three levels by considering physical and geometric constraints, and the detailed conditions are presented in Table 1. The outer diameter of the spring structure was fixed at 6 mm to maintain geometric consistency with the conventional cylindrical fin. Accordingly, the inner diameter of the spring was determined by the wire diameter, which was established within the range of 1 mm to 2 mm by considering structural stability and manufacturability. The height of the spring structure was limited to the range of 10 mm to 50 mm so that the total height of the reference fin, which was 50 mm, would not be exceeded. In addition, when the height of the spring structure did not reach the total fin height, the lower section corresponding to the insufficient length was composed of a conventional cylindrical structure, such that the overall fin height consisting of the spring and cylindrical sections was maintained at a constant value of 50 mm. Through this design, the effect of the spring structure could be compared under all design conditions while maintaining the same reference height. Meanwhile, the pitch spacing of the spring structure was established to be at least 2.2 mm in order to prevent physical contact between adjacent coils and to secure flow passages. These constraints were considered to prevent structural interference while allowing natural convection flow to be smoothly developed.

3. Experimental method

Fig. 3 shows a photograph of the fabricated pin fin heatsink in which a spring structure was combined with the upper section of the cylindrical fin. The spring structure was fabricated using aluminum wire with a diameter of 1.25 mm, and the wire was wound onto a 3D-printed winding jig to precisely realize the optimized pitch and height. The fabricated spring was fixed by a mechanical crimping method such that the lower end of the spring was brought into close contact with the upper section of the fin. During this process, thermal grease was coated on the interface between the spring and cylindrical section in order to minimize contact thermal resistance.

Fig. 4 illustrates the schematic diagram of the experimental apparatus and the temperature measurement locations used for evaluating the heatsink thermal resistance. A film heater (WKH0808-H, WATTREIN, Gimpo, Korea) measuring 75 mm × 75 mm was placed on the bottom surface of the heatsink base, and constant electrical power ranging from 5 to 30 W was supplied using a DC power supply (MK 6005P, MKPOWER, Seoul, Korea). Beneath the film heater, a Bakelite insulator ($\rho = 1300$ kg/m^3, $k = 0.223$ W/m·K, and $C_p = 920$ J/kg·K) measuring 80 mm × 80 mm × 80 mm was installed to minimize heat loss. In addition, thermal grease was uniformly coated on the contact interfaces between the heatsink base and film heater, as well as between the film heater and insulator, in order to minimize contact thermal resistance caused by microscopic air gaps and to ensure that the heat generated from the heater was

Table 1
Ranges and levels of spring structure design variables for the Response Surface Methodology analysis.

Factors	Levels		
	Minimum value	Middle value	Maximum value
Wire diameter, x_1 (mm)	1	1.5	2
Spring height, x_2 (mm)	10	30	50
Spring pitch, x_3 (mm)	2.2	3.1	4



Fig. 3. Photograph of the fabricated pin-fin heatsink with fins composed of a cylindrical lower section and an aluminum wire spring upper section.

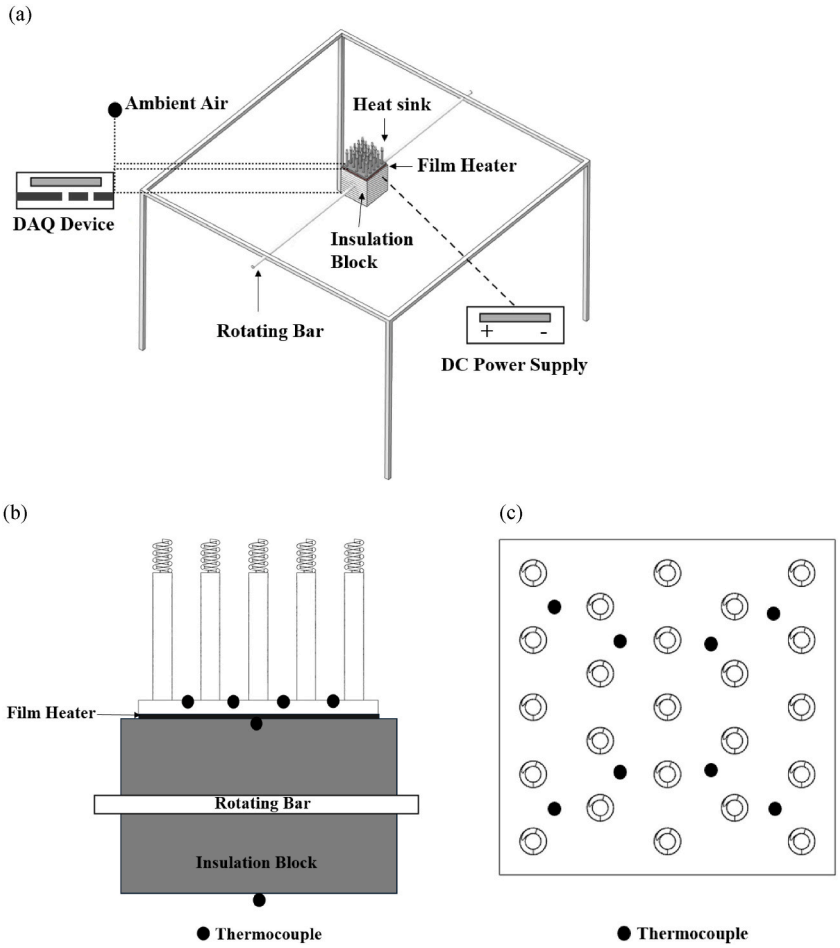


Fig. 4. Schematic of the experimental apparatus: (a) overall setup, (b) thermocouple locations (side view), (c) thermocouple locations (top view).

transferred to the base without loss. A rotating bar penetrating horizontally through the center of the insulator was connected to the table, thereby allowing the heatsink installation angle to be adjusted. T-type thermocouples were employed for temperature measurements, and temperatures were detected at eight positions on the upper surface of the heatsink base, one location at the center between the film heater and the lower surface of the base, one location at the center of the lower surface of the insulator for evaluating heat loss, and one location in the ambient air. The experiments were conducted under an ambient air temperature maintained at 300 K using an air conditioner, and partitions were installed with a sufficiently large distance from the heatsink to minimize the influence of external airflow. More than approximately 30 min was required to reach steady-state conditions at all measurement locations where no

further temperature variation was observed, and the temperatures at each location were subsequently recorded. To ensure the reproducibility of the experiments, the entire experiment was repeated three times under identical conditions. The thermal resistance (R_{th}) of the heatsink was determined by Eq. (5) [41]. Here, $T_{sink,avg}$ and T_∞ denote the average heatsink temperature measured at the eight locations and the ambient air temperature, respectively. V and I represent the voltage and current supplied to the heater, while k_{ins}, A_{ins}, and H_{ins} denote the thermal conductivity, cross-sectional area, and height of the Bakelite insulator, respectively. In addition, $T_{sink,bot}$ represents the temperature at the lower surface of the heatsink base, and $T_{ins,bot}$ represents the temperature at the lower surface of the insulator.

$$R_{th} = \frac{T_{sink,avg} - T_\infty}{VI - \left(\frac{k_{ins}A_{ins}}{H_{ins}}\right)\left(T_{sink,bot} - T_{ins,bot}\right)} \tag{5}$$

4. Results and discussion

Fig. 5 presents the temperature distributions of the heatsink for several selected cases according to the principal design variables of the spring wire configuration, including diameter, height, and pitch, under a heat input condition of 30 W. Fig. 5(a) shows the case in which the fins were composed only of a spring structure without a cylindrical lower section. In this case, the heat generated from the base was not effectively transferred to the upper section of the fins and tended to be concentrated near the lower region. As a result, relatively high temperatures were formed throughout the heatsink base, indicating that the corresponding structure was inefficient in terms of heat transfer path. In contrast, for the cases displayed in Fig. 5(b) and (c), in which a cylindrical structure of a certain length was included at the lower section of the fin, the heat transferred from the base was more effectively delivered to the upper section of the spring structure. Consequently, the overall temperature of the heatsink base was less than that shown in Fig. 5(a), suggesting that the cylindrical lower section supplemented the heat transfer path and contributed to the enhancement of heat dissipation performance.

Meanwhile, since the wire diameter and pitch have been reported as major parameters significantly affecting the airflow inside the spring structure and between adjacent springs [32], an optimal design based on the Response Surface Methodology (RSM) combined with the Box–Behnken Design (BBD) was performed in the present study by considering these geometric variables [47,48]. Table 2 summarizes a total of 15 analysis conditions constructed at three levels using BBD for the three design variables of the spring configuration, namely spring pitch x_3, spring height x_2, and wire diameter x_1, together with the simulation outcomes of R_{th} for each condition under the 30 W heat input condition. In the present study, the spring structure was optimized using thermal resistance as a single objective function. However, mass, material usage, manufacturability, and structural stability should also be considered as important design factors for practical heatsink applications. Therefore, a multi-objective optimization incorporating these factors

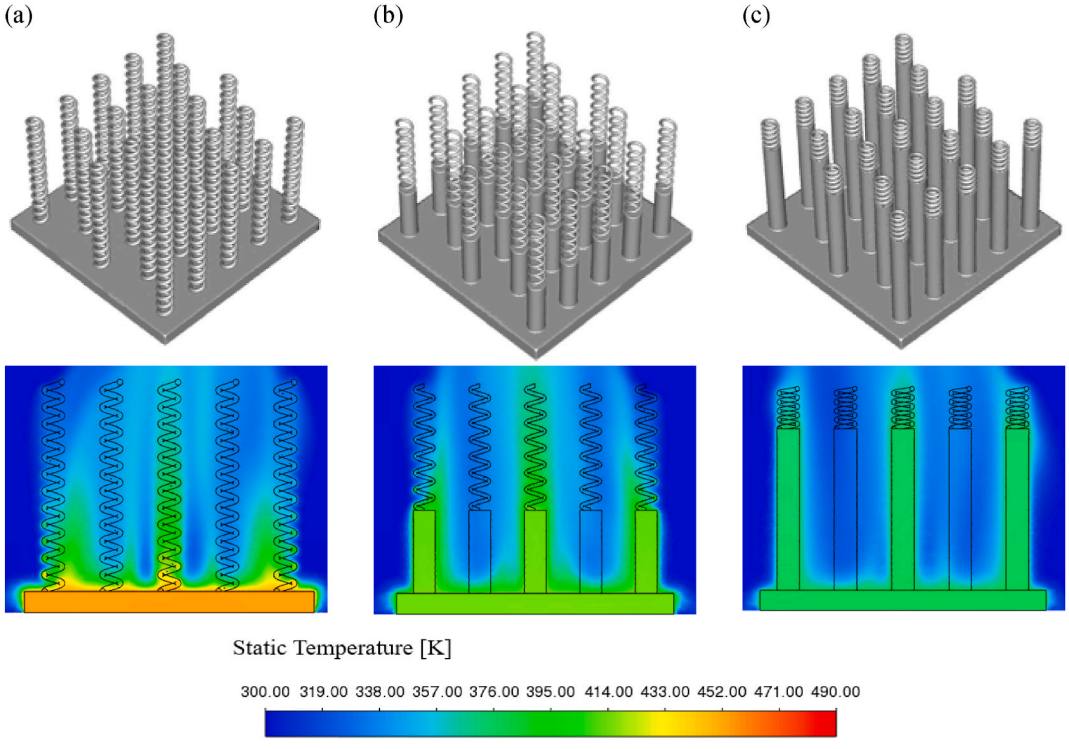


Fig. 5. Comparison of temperature contours with a temperature scale range from 300 to 490 K under a heat input of 30 W for selected spring wire design parameters: (a) d = 1.5 mm, h = 50 mm, p = 4 mm; (b) d = 1.0 mm, h = 30 mm, p = 4 mm; (c) d = 1.25 mm, h = 10 mm, p = 2.2 mm.

Table 2
Box–Behnken design matrix and corresponding thermal resistance (R_{th}) values at a heat input of 30 W.

Number	x_1 (mm)	x_2 (mm)	x_3 (mm)	R_{th} (K/W)
1	2	10	3.1	2.557
2	1	10	3.1	2.512
3	2	50	3.1	2.905
4	1	50	3.1	3.185
5	2	30	4	2.855
6	1.5	50	2.2	2.843
7	1.5	10	4	2.733
8	2	30	2.2	2.756
9	1.5	50	4	3.061
10	1	30	2.2	2.889
11	1.5	30	3.1	2.826
12	1.5	30	3.1	2.826
13	1	30	4	3.142
14	1.5	10	2.2	2.553
15	1.5	30	3.1	2.826

should be performed in future studies.

Table 3 presents the analysis of variance (ANOVA) results performed based on the R_{th} results listed in Table 2. The F-value and P-value of the overall regression model were found to be 11.83 and 0.007, respectively, meaning that the proposed regression model could statistically explain the variation in the response values with significance. Among the principal design variables, the spring height x_2 was identified as the most influential parameter, showing an F-value of 67.58 and a P-value of less than 0.001. This result indicates that the spring height plays a dominant role in natural convection heat transfer and thermal resistance variation. Eq. (6) represents the response surface regression equation derived in the present study. In the regression equation, the sign of each coefficient indicates the effect of the design variable variation on thermal resistance. A minus sign implies a contribution to thermal resistance reduction, whereas a plus sign reflects a contribution to thermal resistance increase. In addition, the coefficient of determination (R^2) of the overall regression model was found to be 95.51%, confirming that the proposed response surface equation effectively explained the variation in thermal resistance.

$$R_{th} = 2.45 - 0.115x_1 + 0.03199x_2 - 0.136x_3 + 0.153{x_1}^2 - 0.000187{x_2}^2 + 0.0569{x_3}^2 - 0.00813x_1x_2 - 0.0856x_1x_3 + 0.00053x_2x_3 \quad (6)$$

Fig. 6 presents the response surfaces showing the influences of the spring geometry design variables on the heatsink thermal resistance. Fig. 6(a) shows the effects of the wire diameter x_1 and spring height x_2 on thermal resistance. With increasing spring height, the thermal resistance generally exhibited an increasing trend. In particular, this increasing tendency became more pronounced under conditions with a smaller wire diameter. This behavior can be interpreted as resulting from the relative reduction in the length of the lower cylindrical section as the spring height increased, thereby preventing the heat generated from the base from being effectively transferred to the upper section of the fin. In contrast, under conditions with a lower spring height, the heat transfer path was relatively short, resulting in only small variations in thermal resistance and generally lower thermal resistance values. In this region, the influence of wire diameter variation was also relatively alleviated. Fig. 6(b) presents the effects of the wire diameter x_1 and spring pitch x_3 on thermal resistance. With an increase in wire diameter, the thermal resistance generally decreased, which can be linked to the enhancement of convective heat transfer induced by the increase in surface area associated with the larger wire diameter. Meanwhile, the smallest thermal resistance values were identified within the pitch range of approximately 2.2–2.4 mm. This behavior is considered to result from the interaction with the wire diameter. When the pitch was excessively small, the inflow of air into the internal space of

Table 3
ANOVA results for the response surface model of thermal resistance based on the results in Table 2.

Parameter	Degree of freedom	Sum of squares	Mean square	F-Value	P-value
Model	9	0.529077	0.058786	11.83	0.007
x_1	1	0.053628	0.053628	10.79	0.022
x_2	1	0.33579	0.33579	67.58	<0.001
x_3	1	0.070312	0.070312	14.15	0.013
$x_1 \times x_1$	1	0.005437	0.005437	1.09	0.343
$x_2 \times x_2$	1	0.020562	0.020562	4.14	0.098
$x_3 \times x_3$	1	0.007855	0.007855	1.58	0.264
$x_1 \times x_2$	1	0.026406	0.026406	5.31	0.069
$x_1 \times x_3$	1	0.005929	0.005929	1.19	0.324
$x_2 \times x_3$	1	0.000361	0.000361	0.07	0.798
Residuals	5	0.024844	0.004969		
Lack of fit	3	0.024844	0.008281		
Pure error	2	0	0		
Total	14	0.553921			

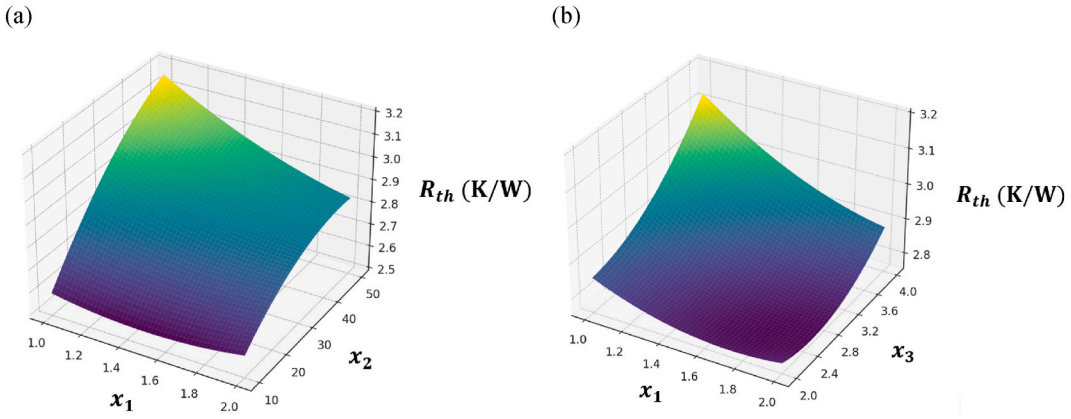


Fig. 6. Response surface plots showing the effects of spring design variables on the thermal resistance (R_{th}) of the heatsink: (a) effects of x_1 and x_2, (b) effects of x_1 and x_3.

the spring was restricted, thereby deteriorating the convective effect. In contrast, when the pitch was excessively high, the flow interaction between neighboring springs was reduced, thereby decreasing the heat transfer enhancement effect.

Table 4 presents the minimum thermal resistance condition derived from the response surface methodology based on the numerical results, together with the corresponding spring geometry parameters. The optimal configuration was derived as a spring pitch of 2.2 mm, spring height of 10 mm, and wire diameter of 1.25 mm. Under this condition, the thermal resistance predicted through the regression model was 2.499 K/W, whereas the numerical analysis result under the same condition was found to be 2.481 K/W. The difference between the two results was approximately 0.72%, indicating good agreement between the RSM prediction and the numerical result at the optimal design condition. Therefore, the response surface model established in the present study was considered suitable for deriving the optimal design and estimating thermal resistance within the investigated design range. Meanwhile, when a pin fin heatsink composed only of cylindrical fins with a height of 50 mm was established as the reference model, the mass and thermal resistance of the corresponding heatsink were found to be 0.159 kg and 2.77 K/W, respectively. In contrast, the pin fin heatsink combined with the spring structure under the optimal design condition presented in Table 4 exhibited reduced thermal resistance and mass values of 2.481 K/W and 0.150 kg, respectively. These results indicate that the thermal resistance decreased by approximately 10.4% while a simultaneous weight reduction of approximately 5.7% was achieved compared with the reference model. These findings demonstrate that the proposed spring structure can simultaneously realize enhancement of heat transfer performance and structural lightweighting.

Fig. 7 compares the local and global flow vector distributions between the reference heatsink with cylindrical pin fins and the optimized heatsink with cylindrical–spring pin fins. Fig. 7(a) and (b) show the local flow around the cylindrical pin fin of the reference model and the cylindrical–spring pin fin of the optimized model, respectively. In the reference model, a simple upward flow structure was formed along the surface of the cylindrical fins. In contrast, in the cylindrical-spring pin fin heatsink, a complex flow structure was observed in which a core flow ascending through the interior of the spring was simultaneously formed together with a side flow induced by external air entering into the spring interior. The formation of such side flow in a helical coil structure has previously been reported as a major factor promoting flow disturbance and fluid mixing, thereby enhancing heat dissipation performance [32]. The complex flow structure identified in the present study is also considered to have promoted heat transfer by activating air mixing between the outside and inside of the spring structure, increasing fluid mixing, and simultaneously enlarging the effective surface area in contact with air. Consequently, these changes in flow characteristics are interpreted to have contributed to the reduction in thermal resistance of the proposed structure. Fig. 7(c) and (d) show the flow distributions at the A–A′ cross-section selected to compare the flow characteristics across the entire pin-fin array. The A–A′ cross-section corresponds to an x–y plane located 45 mm above the heatsink base plate. In the reference model, the flow between the fins was relatively uniformly distributed, whereas in the optimized cylindrical–spring pin fin model, more pronounced flow interactions between adjacent fins and airflow toward the central region of the heatsink were observed due to the spring structures. These results indicate that the local flow modifications induced around individual spring fins also affected the overall flow distribution across the staggered array.

Fig. 8 presents the comparison of the average upward velocity predicted through numerical analysis in the upper fin region between the reference model and the optimized cylindrical-spring pin fin model when the installation angle of the heatsink was 0°. The upward velocity was evaluated in the region near the upper section of the pin fins, and the measurement locations from P1 to P6 were established at a total of six positions by dividing the height range from 40 mm to 50 mm above the heatsink base surface at intervals of

Table 4
Optimal spring design variables and corresponding thermal resistance (R_{th}) values.

Parameter	x_1 (mm)	x_2 (mm)	x_3 (mm)	R_{th} (RSM prediction, K/W)	R_{th} (CFD, K/W)
Value	1.25	10	2.2	2.499	2.481

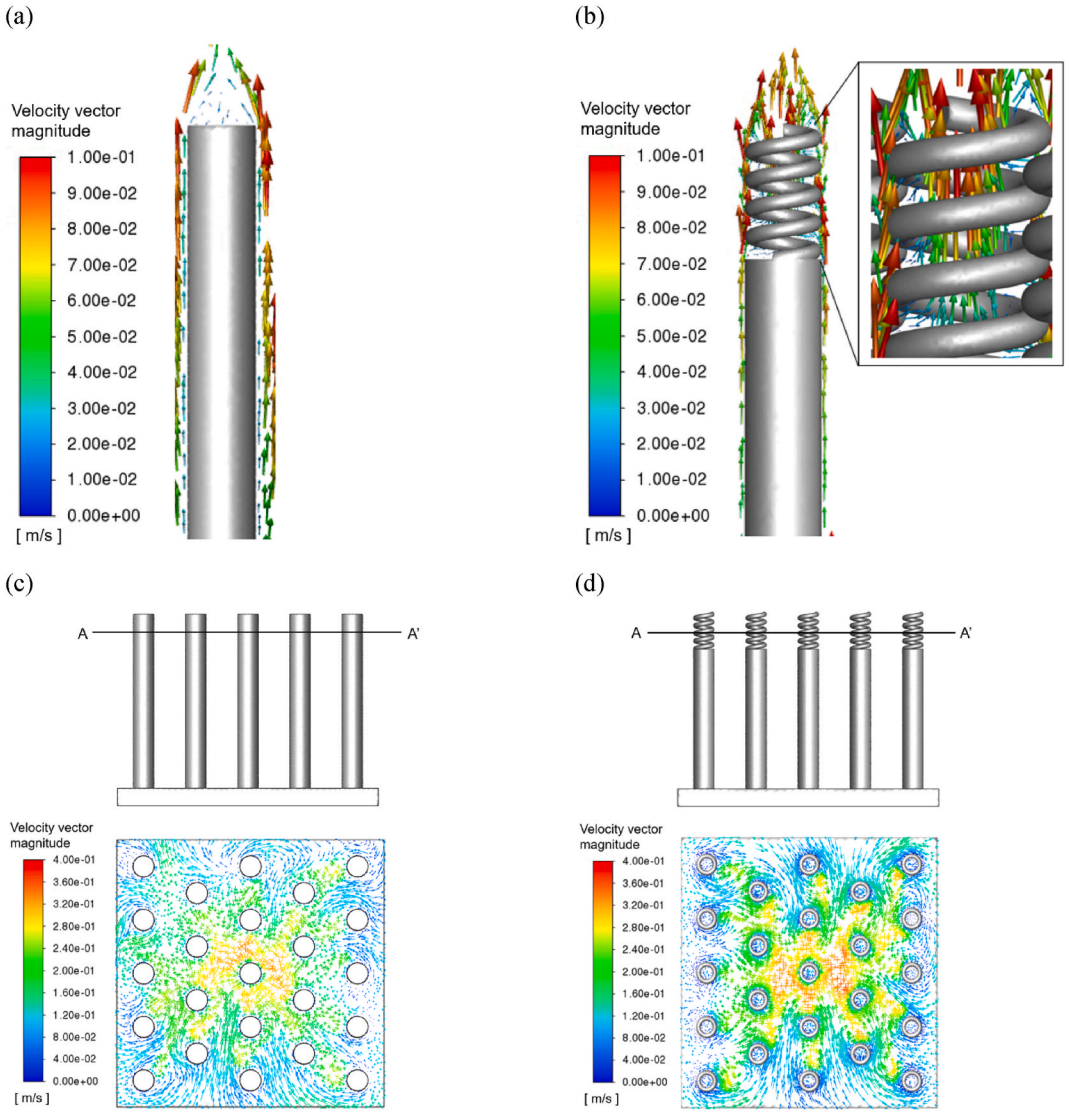


Fig. 7. Comparison of velocity vector distributions between the reference heatsink with cylindrical pin fins and the optimized heatsink with cylindrical–spring pin fins: (a) local flow around a cylindrical pin fin in the reference heatsink, (b) local flow around a cylindrical–spring pin fin in the optimized heatsink, (c) flow distribution at the A–A′ cross-section of the reference heatsink, (d) flow distribution at the A–A′ cross-section of the optimized heatsink.

2 mm. At each location, the average velocity on the horizontal plane corresponding to the specified height was calculated. As presented in Fig. 8(b), the reference model exhibited a tendency in which the upward velocity gradually increased with increasing height and then converged toward an approximately constant value. In contrast, in the optimized cylindrical-spring pin fin model, the upward airflow velocity continuously increased as the measurement position became higher. In particular, at the uppermost position P6, the upward velocities of the reference model and the optimized cylindrical-spring pin fin model were found to be 0.0763 m/s and 0.0841 m/s, respectively, indicating an approximately 10.2% higher upward velocity in the optimized model. This difference is interpreted as resulting from the side flow generated within the spring structure interacting with the internal core flow, thereby enhancing flow mixing and inducing progressive acceleration of the upward airflow. This observation aligns with the complex flow characteristics identified in the previous flow structure analysis and is therefore considered to be a major factor contributing to the enhancement of cooling performance.

Fig. 9 displays the numerical analysis outcomes comparing the convective heat transfer coefficients between the optimized cylindrical-spring pin fin model and the reference model according to variations in the heatsink installation angle. As the power supplied to the heatsink base was gradually varied from 5 W to 30 W, thereby changing ΔT, which represents the gap between the average base temperature and the ambient fluid temperature, the difference in convective heat transfer coefficient between the two models was found to be relatively small under low power conditions. This behavior is interpreted as resulting from the insufficient

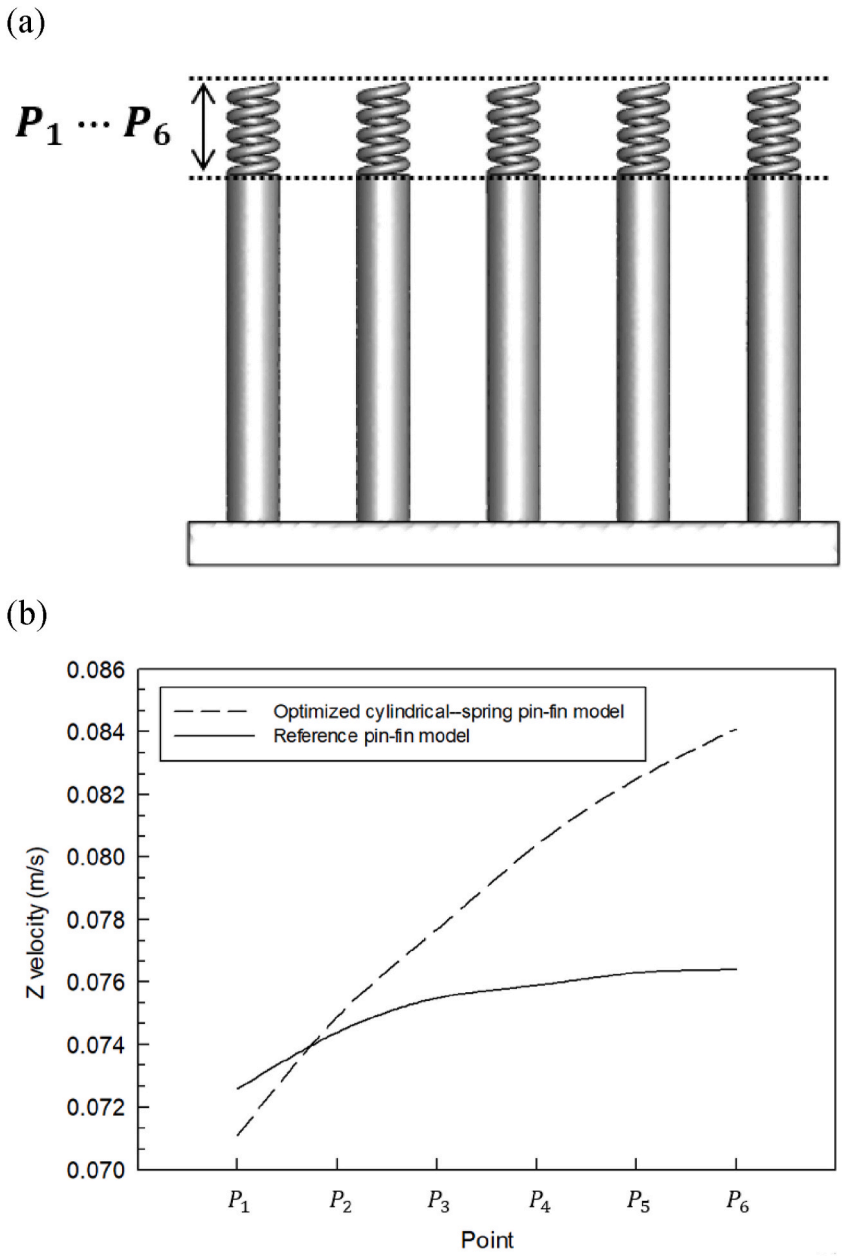


Fig. 8. Comparison between the reference and optimally designed cylindrical–spring pin-fin heatsinks at an installation angle of 0°: (a) measurement locations, (b) comparison of average upward velocities.

velocity of the upward airflow generated by natural convection, which limited the flow disturbance and heat transfer enhancement effects induced by the spring structure. In contrast, as the applied power increased, ΔT became larger and the natural convection effect was strengthened. Consequently, in the optimized cylindrical-spring pin fin model, the interaction with the surrounding fluid became more active, resulting in a more pronounced enhancement of heat transfer performance relative to the reference model. In particular, under the installation angle condition of 90°, the fins were arranged horizontally, enabling the fluid to smoothly pass through the spaces between the fins. As a result, the stagnant region was reduced, and both models exhibited relatively higher convective heat transfer coefficients compared with those at other installation angles. Conversely, under the installation angle condition of 180°, the heatsink was arranged in an inverted configuration with the base located at the upper side, thereby restricting the formation of upward airflow. Accordingly, both models exhibited degraded heat transfer performance under this condition. Nevertheless, the optimized cylindrical-spring pin fin model maintained higher convective heat transfer coefficients than the reference model under all installation angle conditions. This behavior is considered to result from the spring structure providing additional heat transfer area while simultaneously forming a complex flow structure that expanded the heat transfer pathways.

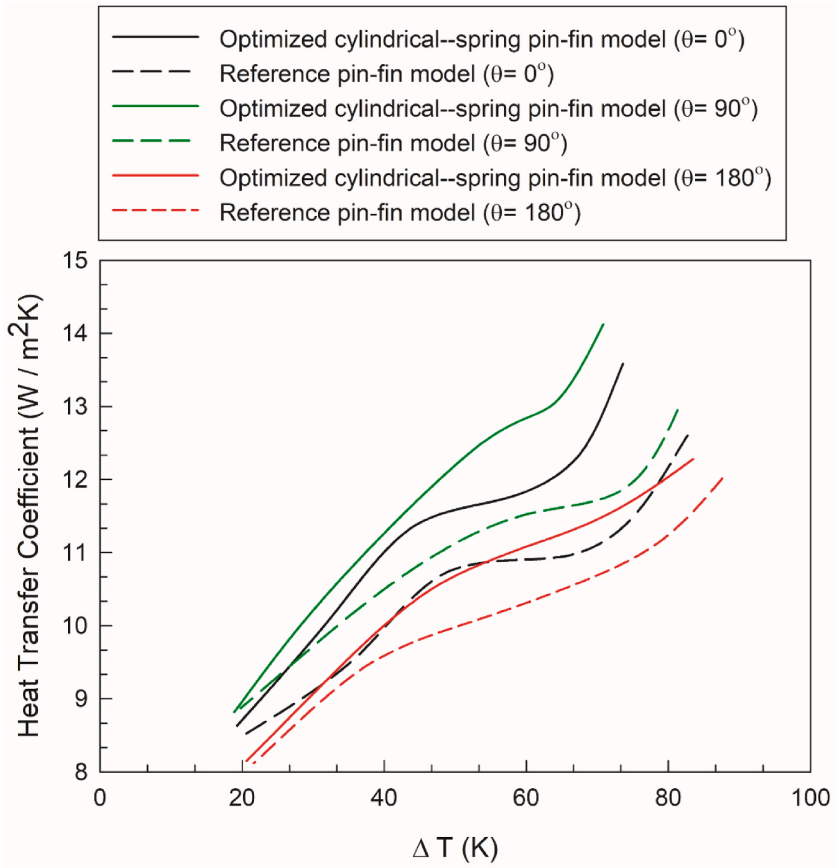


Fig. 9. Comparison of convective heat transfer coefficients between the reference and optimized cylindrical–spring pin-fin heatsinks at different installation angles.

Fig. 10 compares the thermal resistance of the heatsink between the experimental and numerical results according to the installation angles of the heatsink (0°, 45°, 90°, 135°, and 180°) and the power applied to the base (5, 10, 15, 20, 25, and 30 W). The experimental validation was conducted for the reference model and the optimized design to confirm the thermal performance improvement achieved by the optimized design derived from the RSM based on numerical data. The error bars in the experimental results represent the combined uncertainty, including the maximum deviation in thermal resistance from repeated experiments and the uncertainties associated with temperature and power measurements. With variation in the installation angle, both models exhibited similar trends in thermal resistance, and the optimized cylindrical-spring pin fin heatsink model showed lower thermal resistance than the reference model under all power conditions. In addition, as the applied power increased, the natural convection effect was strengthened, and the thermal resistance generally exhibited a decreasing tendency. This tendency was consistent with the previously presented numerical results of the convection heat transfer coefficient. Considering the effect of installation angle, the thermal resistance in both models gradually decreased as the angle increased from 0° to 90°, reaching the minimum value at 90°. This behavior resulted from the most effective formation of upward airflow under the vertical arrangement condition. Thereafter, as the installation angle further increased to 180°, the thermal resistance increased again, which is interpreted as resulting from the restriction of upward airflow formation in the inverted heatsink arrangement. Quantitatively, under the applied power condition of 30 W, the thermal resistance of the optimized cylindrical-spring pin fin heatsink model reached the minimum level of 2.46 K/W at the installation angle of 90°, whereas it increased to 2.80 K/W at 180°, corresponding to an increase of approximately 13.8%. The reference model also exhibited a similar tendency, with the thermal resistance increasing from 2.70 K/W at 90° to 2.96 K/W at 180°, corresponding to an increase of approximately 9.6%. From these results, although the degree of performance degradation under the 180° condition was greater in the optimized cylindrical-spring pin fin heatsink model, the thermal resistance remained lower than that of the reference model, thereby confirming the improved heat dissipation performance. Although mechanical crimping and thermal grease were applied at the interface between the spring and cylindrical fin to minimize contact thermal resistance, a certain degree of contact thermal resistance may have remained due to surface roughness and imperfect contact. In the numerical analysis, perfect thermal contact between the two components was assumed, and thus the contact thermal resistance at the interface was not considered. This assumption may have partly contributed to the discrepancy between the numerical and experimental results. Nevertheless, the numerical and experimental outcomes matched well with an error of less than 5.14%, and the experimental

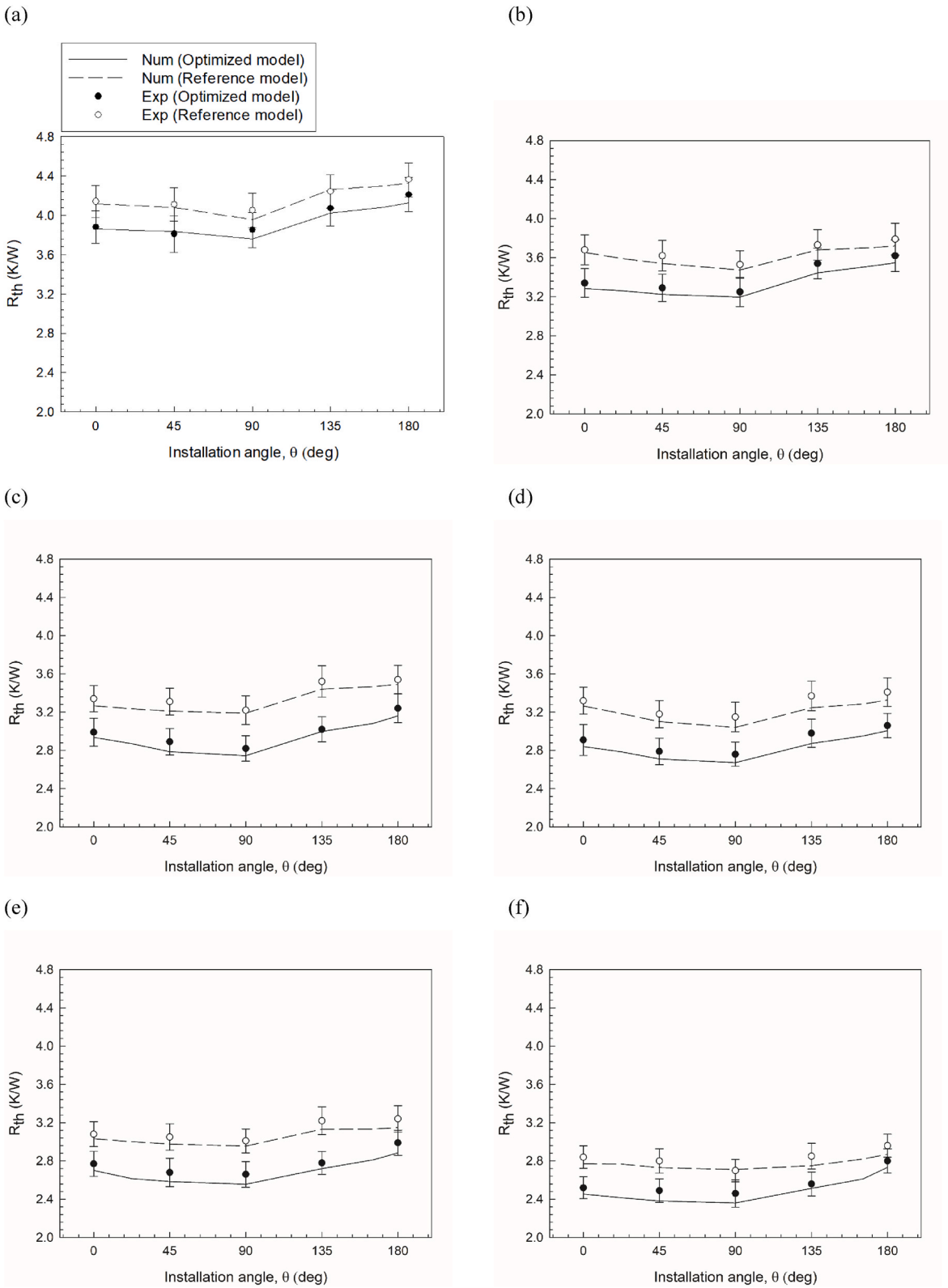


Fig. 10. Comparison of experimental and simulated thermal resistance (R_{th}) as a function of installation angle (θ) at different input power levels: (a) 5 W, (b) 10 W, (c) 15 W, (d) 20 W, (e) 25 W, (f) 30 W.

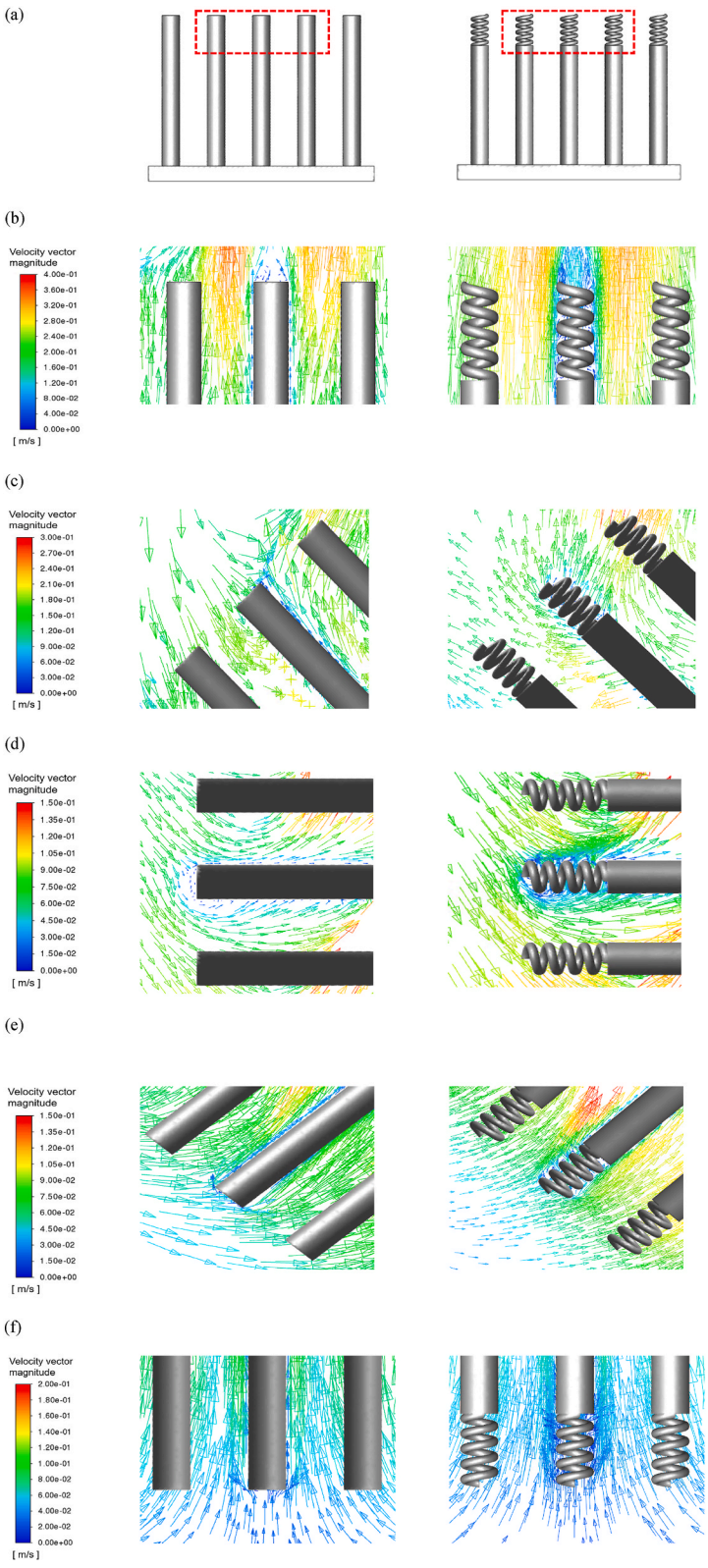


Fig. 11. Comparison of flow fields around the heatsink at an input power of 30 W for different installation angles: (a) flow-field comparison region between the reference pin-fin model and the optimized cylindrical-spring pin-fin model, (b) $\theta = 0°$, (c) $\theta = 45°$, (d) $\theta = 90°$, (e) $\theta = 135°$, (f) $\theta = 180°$.

uncertainty quantified using the approach proposed by Figliola and Beasley [49] was found to be a maximum of 5.83%. Among these, the maximum deviation in thermal resistance obtained from repeated measurements was approximately 4.47%, while the uncertainties associated with temperature and power measurements were evaluated to be up to approximately 3.65% and 0.84%, respectively. These results indicate reasonable agreement between the numerical and experimental results obtained in this study.

Fig. 11 presents the comparison of flow vectors around the optimized cylindrical-spring pin fin heatsink model and the reference model according to variations in the heatsink installation angle under the applied power condition of 30 W. When the installation angle ranged from 0° to 135°, a complex flow structure centered around the spring region was observed in the optimized cylindrical-spring pin fin heatsink model, which appeared as a distinctive feature differentiating it from the reference model. On the other hand, in the middle region of the fins having a cylindrical exterior shape, similar flow distributions were observed in both models. These results indicate that the spring structure caused local flow disturbances, thereby increasing the upward airflow velocity and contributing to the reduction in thermal resistance. However, under the installation angle condition of 180°, different flow characteristics were observed. In the optimized cylindrical-spring pin fin heatsink model, the upward airflow around the spring structure was weakened compared with that in the reference model, resulting in a tendency for the development of airflow to become restricted. This behavior is considered to result from the inability of the buoyancy-induced upward flow to be effectively guided by the spring structure as the installation angle changed to 180°, thereby increasing the flow resistance within the flow passage. This relatively low-velocity flow region extended to the cylindrical body section of the fin, ultimately leading to an overall reduction in the flow velocity around the fins. Therefore, although the spring structure contributed to flow enhancement and heat transfer improvement under most installation angle conditions, it was confirmed that the structure could instead act as a flow resistance element under specific conditions such as 180°. These variations in flow characteristics clearly explain the result shown in Fig. 10, in which the increase in thermal resistance under the 180° installation angle condition was greater for the optimized cylindrical-spring pin fin heatsink model than for the reference model. Nevertheless, since the increased heat transfer area provided by the spring structure and the local flow disturbance effect around the spring end region were still maintained, the thermal resistance remained lower than that of the reference model.

5. Conclusion

In this study, a novel cylindrical-spring pin fin heatsink model in which the upper section of a conventional cylindrical pin-fin heatsink was replaced with a spring structure was proposed, and its cooling performance under free convection conditions was comprehensively investigated through numerical and experimental analyses. Unlike conventional hollow or perforated structures, the proposed configuration possesses a distinct advantage in that flow paths and increased specific surface area can be actively achieved through a simple spring attachment method without requiring complex manufacturing processes. Therefore, the proposed structure was intended to simultaneously achieve structural simplicity, weight reduction, and enhancement of heat dissipation performance. From the optimal design results obtained using the RSM, the spring height was identified as the most dominant parameter affecting the thermal resistance, and the optimal design configuration was determined as a spring pitch of 2.2 mm, spring height of 10 mm, and wire diameter of 1.25 mm. Under this condition, the difference between the thermal resistance predicted by the RSM model (2.499 K/W) and that obtained from numerical analysis (2.481 K/W) was only 0.72%, indicating good agreement between the RSM prediction and the numerical result at the optimal design condition. In addition, compared with the reference heatsink model equipped only with cylindrical fins, the optimized cylindrical-spring pin fin heatsink model simultaneously achieved a thermal resistance reduction of approximately 10.4% and a weight reduction of approximately 5.7%. From the analysis of the flow and heat transfer characteristics according to the installation of the spring structure, it was confirmed that the spring structure formed a complex flow composed of internal core flow and external side flow, thereby promoting fluid mixing and accelerating the upward airflow. Meanwhile, from the analysis of the performance according to variations in installation angle and applied power, both models exhibited the lowest thermal resistance at the installation angle of 90°, where the upward airflow induced by natural convection was most effectively developed. In contrast, under the 180° condition, the development of upward airflow became restricted, resulting in an increase in thermal resistance. In particular, the optimized cylindrical-spring pin fin heatsink model exhibited a larger increase in thermal resistance than the reference model under the 180° condition, indicating that the spring structure could act as a flow resistance element rather than a flow enhancement structure under specific conditions. This tendency was also consistently observed in the flow field analysis results. Nevertheless, owing to the enlarged heat transfer area provided by the spring structure and the local flow disturbance generated around the spring end region, the optimized cylindrical-spring pin fin heatsink model still exhibited lower thermal resistance than the reference model even under the installation angle of 180°. Therefore, enhanced heat dissipation performance was achieved across the full installation angle range from 0° to 180°. The numerical and experimental results showed good agreement within a maximum error of 5.14%, and the maximum experimental uncertainty was evaluated as 5.83%, supporting the validity of the numerical predictions for the experimentally investigated conditions. Overall, the cylindrical-spring pin fin heatsink introduced in this study is considered to be an effective design approach capable of simultaneously achieving enhancement of heat transfer performance and weight reduction through active control of the flow structure by only a simple structural modification. Therefore, the proposed structure possesses high potential for application in various fields requiring both lightweight characteristics and highly efficient thermal management, such as LED lighting and portable electronic devices.

However, several limitations should be acknowledged. Contact thermal resistance at the spring–cylindrical fin interface was not considered in the numerical analysis, and manufacturing and assembly tolerances may affect performance repeatability. As observed in the present study, the heat dissipation performance of the proposed spring structure also varied with the installation angle, indicating that the installation orientation should be considered in practical applications. Experimental validation was limited to the reference model and the optimized design. Furthermore, the present study focused on thermal performance under steady-state

conditions, and the transient thermal response associated with differences in thermal inertia between the spring structure and conventional cylindrical fins was not considered. Long-term mechanical durability was also not evaluated. Under practical operating conditions, repeated vibrations may affect the stability of the mechanical crimping interface and cause spring deformation, while repeated thermal cycles may degrade the thermal grease and increase contact thermal resistance. Therefore, further studies should evaluate the transient thermal response and long-term thermal and structural reliability of the proposed structure, including the effects of contact thermal resistance, manufacturing and assembly tolerances, repeated vibrations, and thermal cycling.

CRediT authorship contribution statement

Hyeon-Min Kang: Writing – original draft, Visualization, Software, Investigation, Formal analysis, Data curation. **Se-Jin Yook:** Writing – review & editing, Validation, Supervision, Resources, Methodology, Funding acquisition, Conceptualization.

Declaration of competing interest

The authors declare that they have no known competing financial interests or personal relationships that could have appeared to influence the work reported in this paper.

Acknowledgment

This work was supported by Korea Environmental Industry & Technology Institute (KEITI) through R&D Program for Fluorinated Greenhouse Gas Mitigation Technologies in Response to International Agreement Project, funded by Korea Ministry of Climate, Energy and Environment (MCEE) (RS-2026-25501408).

Data availability

Data will be made available on request.

References

[1] J.D. Bergesen, L. Tähkämö, T. Gibon, S. Suh, Potential long-term global environmental implications of efficient light-source technologies, J. Ind. Ecol. 20 (2016) 263–275, https://doi.org/10.1111/jiec.12342.
[2] M. Bessho, K. Shimizu, Latest trends in LED lighting, Electron, Commun. Jpn. 95 (2012) 1–7, https://doi.org/10.1002/ecj.10394.
[3] E.F. Schubert, J.K. Kim, Solid-state light sources getting smart, Science 308 (2005) 1274–1278, https://doi.org/10.1126/science.1108712.
[4] M. Hamidnia, Y. Luo, X.D. Wang, Application of micro/nano technology for thermal management of high power LED packaging–A review, Appl. Therm. Eng. 145 (2018) 637–651, https://doi.org/10.1016/j.applthermaleng.2018.09.078.
[5] H. Ye, G. Zhang, A review of passive thermal management of LED module, J. Semicond. 32 (2011) 014008, https://doi.org/10.1088/1674-4926/32/1/014008.
[6] X. Lin, S. Mo, B. Mo, L. Jia, Y. Chen, Z. Cheng, Thermal management of high-power LED based on thermoelectric cooler and nanofluid-cooled microchannel heat sink, Appl. Therm. Eng. 172 (2020) 115165, https://doi.org/10.1016/j.applthermaleng.2020.115165.
[7] C.J. Weng, Advanced thermal enhancement and management of LED packages, Int. Commun. Heat Mass Transf. 36 (2009) 245–248, https://doi.org/10.1016/j.icheatmasstransfer.2008.11.015.
[8] S.J. Wu, H.C. Hsu, S.L. Fu, J.N. Yeh, Numerical simulation of high power LED heat-dissipating system, Electron, Mater. Lett. 10 (2014) 497–502, https://doi.org/10.1007/s13391-014-8003-9.
[9] H.H. Cheng, D.S. Huang, M.T. Lin, Heat dissipation design and analysis of high power LED array using the finite element method, Microelectron. Reliab. 52 (2012) 905–911, https://doi.org/10.1016/j.microrel.2011.05.009.
[10] S. Meganathan, R. Arunkumar, A. Ponshanmugakumar, Numerical analysis of passive heat sink for different shapes, Mater. Today Proc. 46 (2021) 3749–3755, https://doi.org/10.1016/j.matpr.2021.02.014.
[11] S.J. Park, D. Jang, S.J. Yook, K.S. Lee, Optimization of a chimney design for cooling efficiency of a radial heat sink in a LED downlight, Energy Convers. Manag. 114 (2016) 180–187, https://doi.org/10.1016/j.enconman.2016.02.024.
[12] B.S. Seo, K.J. Lee, J.K. Yang, Y.S. Cho, D.H. Park, Development and characterization of optimum heat sink for 30 W chip on board LED down-light, Trans. Electr. Electron. Mater. 13 (2012) 292–296, https://doi.org/10.4313/TEEM.2012.13.6.292.
[13] R. Tucker, M. Khatamifar, W. Lin, K. McDonald, Experimental investigation of orientation and geometry effect on additive manufactured aluminium LED heat sinks under natural convection, Therm. Sci. Eng. Prog. 23 (2021) 100918, https://doi.org/10.1016/j.tsep.2021.100918.
[14] X.R. Meng, X.L. Ma, J.F. Lu, X.L. Wei, A study on improving in natural convection heat transfer for heat sink of high power LEDs, Adv. Mater. Res. 383–390 (2012) 6834–6839. https://doi.org/10.4028/www.scientific.net/AMR.383-390.6834.
[15] Y. Jiu, H. Fan, W. Wang, Investigation of a novel natural convection heat sink for LEDs based on U-shaped mini-heat pipe arrays, Appl. Therm. Eng. 204 (2022) 118000, https://doi.org/10.1016/j.applthermaleng.2021.118000.
[16] Y. Huang, S. Shen, H. Li, Y. Gu, Numerical analysis on the thermal performances of different types of fin heat sink for high-power LED lamp cooling, Therm. Sci. 23 (2019) 625–636, https://doi.org/10.2298/TSCI170623233H.
[17] C. Alvin, W. Chu, C.H. Cheng, J.T. Teng, Thermal analysis of extruded aluminum fin heat sink for LED cooling application, Proc. 6th Int. Microsyst. Packag. Assem. Circuits Technol. Conf. (2011) 397–400, https://doi.org/10.1109/IMPACT.2011.6117207.
[18] H.C. Hsu, Y.C. Huang, Numerical simulation and experimental validation for the thermal analysis of a compact LED recessed downlight with heat sink design, Appl. Sci. 7 (2016) 4, https://doi.org/10.3390/app7010004.
[19] E. Cuce, P.M. Cuce, T. Guclu, A novel passive cooling configuration for photovoltaic panels based on bio-inspired heatsinks and nanoparticle-enhanced PCM, Appl. Therm. Eng. 292 (2026) 130312, https://doi.org/10.1016/j.applthermaleng.2026.130312.
[20] N. Ali, S. Srivastava, I. Haque, J. Yadav, T. Alam, T.U. Siddiqui, M.I.H. Siddiqui, E. Cuce, Heat dissipation and fluid flow in micro-channel heat sink equipped with semi-elliptical pin-fin structures: a numerical study, Int. Commun. Heat Mass Transf. 155 (2024) 107492, https://doi.org/10.1016/j.icheatmasstransfer.2024.107492.
[21] P.M. Cuce, E. Cuce, Optimization of configurations to enhance heat transfer from a longitudinal fin exposed to natural convection and radiation, Int. J. Low-Carbon Technol. 9 (2014) 305–310, https://doi.org/10.1093/ijlct/ctt005.
[22] K.S. Arjun, R. Kumar, Optimization of micro pin-fin heat sink with staggered arrangement, Therm. Sci. 22 (2018) 2919–2931, https://doi.org/10.2298/TSCI161221202A.

[23] K.A.M. Annuar, F.S. Ismail, Optimal pin fin arrangement of heat sink design and thermal analysis for central processing unit, Proc. 5th Int. Conf. Intell. Adv. Syst. (2014) 1–5, https://doi.org/10.1109/ICIAS.2014.6869537.
[24] H.M. Ali, W. Arshad, Effect of channel angle of pin-fin heat sink on heat transfer performance using water based graphene nanoplatelets nanofluids, Int. J. Heat Mass Transf. 106 (2017) 465–472, https://doi.org/10.1016/j.ijheatmasstransfer.2016.08.061.
[25] A.A. Sertkaya, M. Ozdemir, E. Canli, Effects of pin fin height, spacing and orientation to natural convection heat transfer for inline pin fin and plate heat sinks by experimental investigation, Int. J. Heat Mass Transf. 177 (2021) 121527, https://doi.org/10.1016/j.ijheatmasstransfer.2021.121527.
[26] G. Sung, H.M. Kang, S.J. Yook, Effect of installing rings on the cooling performance of a pin fin heatsink, Int. J. Therm. Sci. 210 (2025) 109660, https://doi.org/10.1016/j.ijthermalsci.2024.109660.
[27] N.S. Effendi, K.J. Kim, Orientation effects on natural convective performance of hybrid fin heat sinks, Appl. Therm. Eng. 123 (2017) 527–536, https://doi.org/10.1016/j.applthermaleng.2017.05.134.
[28] S.J. Park, D. Jang, K.S. Lee, Thermal performance improvement of a radial heat sink with a hollow cylinder for LED downlight applications, Int. J. Heat Mass Transf. 89 (2015) 1184–1189, https://doi.org/10.1016/j.ijheatmasstransfer.2015.06.037.
[29] C.H. Huang, K.J. Chung, Optimal design of perforated fins for LED radial heat sink module with varied hole numbers and sizes, Appl. Therm. Eng. 242 (2024) 122451, https://doi.org/10.1016/j.applthermaleng.2024.122451.
[30] X. Meng, J. Zhu, X. Wei, Y. Yan, Natural convection heat transfer of a straight-fin heat sink, Int. J. Heat Mass Transf. 123 (2018) 561–568, https://doi.org/10.1016/j.ijheatmasstransfer.2018.03.002.
[31] E.A.M. Elshafei, Natural convection heat transfer from a heat sink with hollow/perforated circular pin fins, Proc. Int. Conf. Therm. Issues Emerg. Technol. (2010) 185–193, https://doi.org/10.1109/THETA.2010.5766397.
[32] G. Biswal, S. Rath, S.K. Dash, Natural convection and radiative heat transfer from constant surface area vertical helical coils: effect of pitch and height, J. Therm. Sci. Eng. Appl. 15 (2023) 031005, https://doi.org/10.1115/1.4056244.
[33] G. Biswal, S.K. Dash, An isothermal constant surface area horizontal helical coil under natural convection and radiative heat loss: a CFD study, Int. Commun. Heat Mass Transf. 145 (2023) 106846, https://doi.org/10.1016/j.icheatmasstransfer.2023.106846.
[34] K.J. Kim, Performance of hybrid fin heat sinks for thermal control of light emitting diode lighting modules, J. Electron. Packag. 136 (2014) 011002, https://doi.org/10.1115/1.4025673.
[35] ANSYS Inc., Ansys Icepak User's Guide, Chapter 40: Theory, Section 40.4.1, the Boussinesq Model, Release 2024 R2, ANSYS Inc., 2024.
[36] M. Montiel González, J. Hinojosa Palafox, C. Estrada Gasca, Numerical study of the Boussinesq approach validity for natural convection and surface thermal radiation in an open cavity, Rev. Mex. Fis. 59 (2013) 594–605. https://www.redalyc.org/pdf/570/57028306014.pdf.
[37] D.B. Kwak, J.H. Noh, S.J. Yook, Natural convection flow around heated disk in cubical enclosure, J. Mech. Sci. Technol. 32 (2018) 2377–2384, https://doi.org/10.1007/s12206-018-0449-5.
[38] A. Abbas, C.C. Wang, Augmentation of natural convection heat sink via using displacement design, Int. J. Heat Mass Transf. 154 (2020) 119757, https://doi.org/10.1016/j.ijheatmasstransfer.2020.119757.
[39] M. Muneeshwaran, M.K. Tsai, C.C. Wang, Heat transfer augmentation of natural convection heat sink through notched fin design, Int. Commun. Heat Mass Transf. 142 (2023) 106676, https://doi.org/10.1016/j.icheatmasstransfer.2023.106676.
[40] B. Li, Y.J. Baik, C. Byon, Enhanced natural convection heat transfer of a chimney-based radial heat sink, Energy Convers. Manag. 108 (2016) 422–428, https://doi.org/10.1016/j.enconman.2015.11.037.
[41] Y.K. Khor, Y.M. Hung, B.K. Lim, On the role of radiation view factor in thermal performance of straight-fin heat sinks, Int. Commun. Heat Mass Transf. 37 (2010) 1087–1095, https://doi.org/10.1016/j.icheatmasstransfer.2010.06.012.
[42] L. Liu, C. Xu, S. Cai, J. Wang, D. Huang, K. Yang, C. Zheng, J. Guo, Research on the damage characteristics of a UAV flight control system irradiated by a continuous laser, Aerospace 12 (2025) 161, https://doi.org/10.3390/aerospace12020161.
[43] S. Sundar, G. Song, M.Z. Zahir, J.S. Jayakumar, S.J. Yook, Performance investigation of radial heat sink with circular base and perforated staggered fins, Int. J. Heat Mass Transf. 143 (2019) 118526, https://doi.org/10.1016/j.ijheatmasstransfer.2019.118526.
[44] M. Lee, G. Park, C. Park, C. Kim, Improvement of grid independence test for computational fluid dynamics model of building based on grid resolution, Adv. Civ. Eng. 2020 (2020) 8827936, https://doi.org/10.1155/2020/8827936.
[45] J. Zhou, M. Hatami, D. Song, D. Jing, Design of microchannel heat sink with wavy channel and its time-efficient optimization with combined RSM and FVM methods, Int. J. Heat Mass Transf. 103 (2016) 715–724, https://doi.org/10.1016/j.ijheatmasstransfer.2016.07.100.
[46] R. Kumar, M. Zunaid, R.S. Mishra, Multi-objective optimization of hydrothermal performance of a porous minichannel heat sink using RSM and NSGA-II algorithm, Int. J. Heat Fluid Flow 110 (2024) 109600, https://doi.org/10.1016/j.ijheatfluidflow.2024.109600.
[47] S.C. Ferreira, R.E. Bruns, H.S. Ferreira, G.D. Matos, J.M. David, G.C. Brandão, W.N.L. Dos Santos, Box-Behnken design: an alternative for the optimization of analytical methods, Anal. Chim. Acta 597 (2007) 179–186, https://doi.org/10.1016/j.aca.2007.07.011.
[48] N. Aslan, Y. Cebeci, Application of Box–Behnken design and response surface methodology for modeling of some Turkish coals, Fuel 86 (2007) 90–97, https://doi.org/10.1016/j.fuel.2006.06.010.
[49] R.S. Figliola, D.E. Beasley, Theory and design for mechanical measurements, Meas. Sci. Technol. 12 (2001) 1743, https://doi.org/10.1088/0957-0233/12/10/701.